Real-Time Manipulation with Magnetically Tunable Structures

Citation: Zhu, Yangying, Dion S. Antao, Rong Xiao, and Evelyn N. Wang. "Real-Time Manipulation with Magnetically Tunable Structures." Advanced Materials, Volume 26, Issue 37, October 8, 2014, Pages: 6442–6446.

As Published: http://dx.doi.org/10.1002/adma.201401515

Publisher: John Wiley & Sons, Inc

Persistent URL: http://hdl.handle.net/1721.1/88536

Version: Author's final manuscript: final author's manuscript post peer review, without publisher's formatting or copy editing

Real-Time Manipulation with Magnetically Tunable Structures

*Yangying Zhu, Dion S. Antao, Rong Xiao, Evelyn N. Wang**

Department of Mechanical Engineering, Massachusetts Institute of Technology, Cambridge, MA 02139, USA
E-mail: enwang@mit.edu

Keywords: tunable surface, dynamic material, magnetic, real-time manipulation, directional wettability

Responsive actuating surfaces have attracted significant attention as promising materials for liquid transport in microfluidics, cell manipulation in biological systems, and light tuning in optical applications *via* their dynamic regulation capability. Significant efforts have focused on fabricating static micro and nanostructured surfaces,[1,2,3,4,5] even with asymmetric features to realize passive functionalities such as directional wettability[6,7] and adhesion.[8,9] Only recent advances in utilizing materials that mechanically respond to thermal,[10,11,12,13] chemical[14,15,16,17] or magnetic[18,19,20,21,22,23] stimuli have enabled dynamic regulation. However the challenges with these surface designs are associated with the tuning range,[19,20] accuracy,[19,20,21,22,23] response time[10,11,12,13,15,16,17] and multi-functionality for advanced systems. Here we report dynamically tunable micropillar arrays with uniform, reversible, continuous and extreme tilt angles with precise control for real-time fluid and optical manipulation. Inspired by hair and motile cilia on animal skin and plant leaves for locomotion,[24] liquid transportation[25] and thermal-optical regulation,[26,27] our flexible uniform responsive microstructures (μFUR) consist of a passive thin elastic skin and active ferromagnetic microhair whose orientation is controlled by a magnetic field. We experimentally show uniform tilt angles ranging from 0° to 57°, and developed a model to accurately capture the tilting behavior. Furthermore, we demonstrate that the μFUR can control and change liquid spreading direction on demand, manipulate fluid drag, and tune optical transmittance over a large range. The versatile surface developed in this work enables

new opportunities for real-time fluid control, cell manipulation, drag reduction and optical tuning in a variety of important engineering systems, including applications that require manipulation of both fluid and optical functions.

Dynamically tunable structured surfaces offer new manipulation capabilities in mechanical, fluidic, and optical systems. Examples from nature have inspired the design of such active systems: bacteria use flagella as propellers[24] and motile cilia in the lining of human respiratory airways move mucus and dirt out of the lungs.[25] These biological systems display well-defined structural patterns and controllable mechanical motion in response to different stimuli. Accordingly, researchers have investigated various approaches to fabricate tunable microstructures including temperature-sensitive liquid crystalline[13] and thermoplastic elastomers,[10] hydrogels that respond to thermal, chemical or optical stimuli,[11,12,14,15,16,17] and polymer-based magnetically actuated structures[18,19,20,21,22,23] over the past decade. However, the response of the thermally actuated elastomer is either irreversible[10] or slow[13] and the hydrogels require a liquid environment and have a long response time, thus limiting their applications.

Magnetically actuated surfaces, on the other hand, are attractive due to their instantaneous response and the non-intrusive nature of magnetic fields. Many of the reported approaches use magnetic particles mixed with or encapsulated by soft materials to form microstructures that deflect in an external magnetic field.[18,19,20,21,22,23] These composite surfaces have been used to apply forces to living cells for different cellular reactions,[19] generate rotational and translational fluid movements in microfluidics,[20,21] as well as manipulate and mix droplets.[22] However due to their low magnetic strength which is limited by the volume fraction of particles in the polymer matrix, the tilt angles were usually small and

non-uniform.[19,20,21] Thus, the tuning capability has generally been limited to on-off control, as opposed to a continuous tuning range which is more desirable. Recently a large tuning range of these composite micropillars has been realized by higher and a more uniform distribution of stronger magnetic particles in the polymer matrix.[23] The surface was used to demonstrate switchable adhesive properties.

Here we present a hybrid approach for the development of flexible uniform responsive microstructures (μFUR, **Figure 1**a) in which a thin elastic polydimethylsiloxane (PDMS) layer serves as the skin and a ferromagnetic micropillar array functions as the tunable hair (Figure 1b). The uniform volumetric properties of the pillars allow high fidelity modeling and uniform tilt angle control. Furthermore, the μFUR completely decouples the mechanical, magnetic, wettability and optical properties of the micropillars and the substrate by the use of the two distinct materials, which expands the functionality where different surface properties are required (Figure 1c). With this design, we demonstrated uniform and continuous tilt angles (Figure 1d, Supporting Information Video 1 and 2) which were captured accurately by our model. In the extreme case where the pillars are in contact with the adjacent ones, the tilt angle reaches a maximum of 57° (Figure 1e). This maximum tilt angle can be further increased by optimizing the pillar spacing. We show that μFUR is capable of *real-time* manipulation of liquid spreading directionality, fluid drag, and optical transmittance.

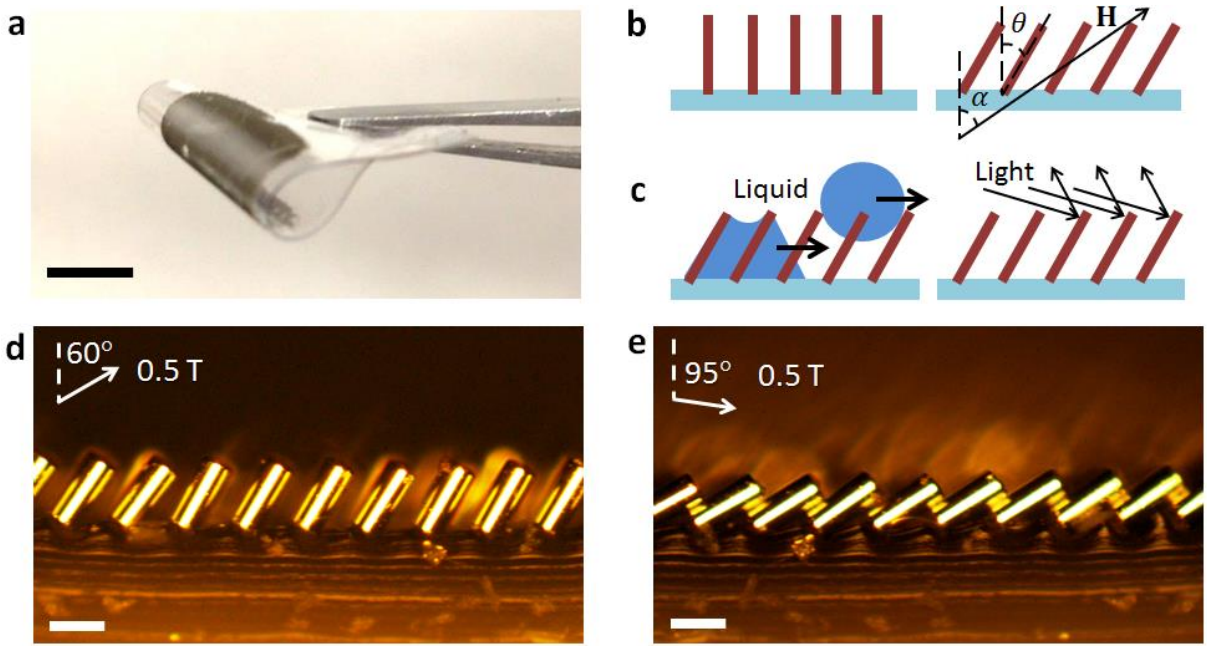

Figure 1. a) The fabricated flexible uniform responsive microstructures (µFUR). The dark region is the micropillar array and the transparent substrate is the PDMS skin. Scale bar is 5 mm. b) Schematic showing the concept of µFUR where the tilt angle can be controlled *via* an external magnetic field. θ is the micropillar tilt angle and α is the magnetic field angle. c) Schematic of potential applications including microfluidic and optical manipulation. Side view images of the fabricated µFUR with an applied magnetic field strength of 0.5 T and field angle of d) $\alpha = 60°$ and e) $\alpha = 95°$ respectively. Scale bars are 50 µm.

The surfaces were created by fabricating ferromagnetic micropillars and then bonding to a soft PDMS substrate as summarized in **Figure 2**a. A dense array of nickel pillars with diameters (d) of 26-30 µm, heights (h) of 70-75 µm, and spacings (l) of 60 µm was electroplated (Figure 2b – 2d). The geometries were chosen due to the ease of fabrication. The nickel posts were subsequently bonded to a PDMS surface through a silica adhesion layer (Figure 2e). The fabrication of µFUR was demonstrated repeatably over an area of 8 mm × 8 mm and can be easily scaled to larger arrays.

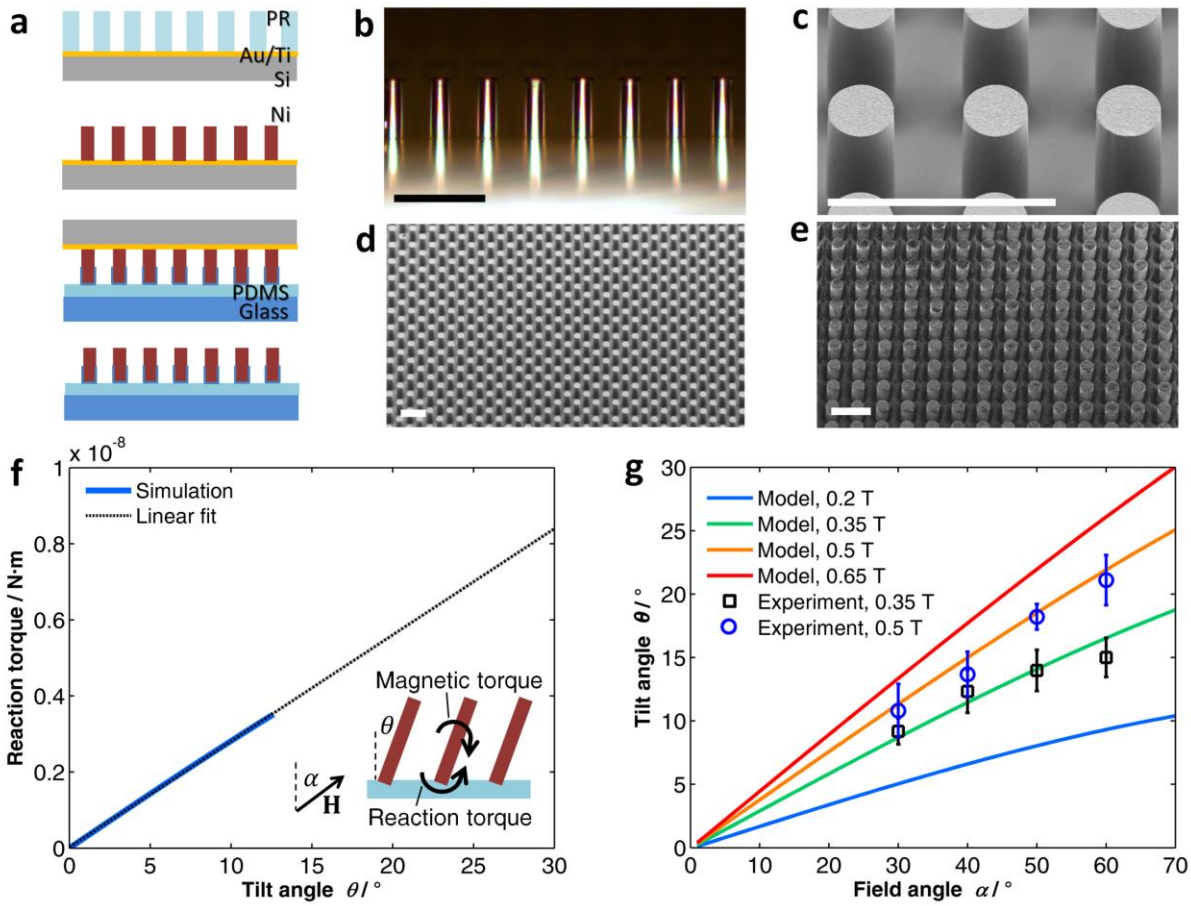

Figure 2. a) Fabrication process flow. First, photoresist was patterned on a gold (Au) seed layer and a titanium (Ti) adhesion layer e-beam evaporated on a silicon (Si) substrate; Second, nickel (Ni) was electroplated inside the photoresist mold and then the photoresist was stripped; Third, the nickel pillars were bonded to PDMS through a silica adhesion layer; Finally, the silicon substrate was detached from the pillars. b) Optical microscope image of the nickel pillar arrays on silicon. c) and d) SEMs of the nickel pillar arrays on silicon. e) SEM of the nickel pillar arrays bonded to PDMS. Scale bars are 100 μm. f) Finite element simulation (Abaqus) results of the reaction torque as a function of the tilt angle when h = 80 μm and d = 26 μm. The solid line is from the simulation and the dotted line is the linear fit. The inset provides a schematic of the torques exerted on the pillars. g) Calculation and experimental results of tilt angle as a function of field strength and field angle. Error bars

account for the standard deviation of multiple measurements (on 30 pillars) and an estimated system error.

With the fabricated pillar geometry and magnetic properties (see Supporting Information Figure S1), we developed a model to predict the equilibrium micropillar tilt angle θ under various magnetic field conditions. The model is based on the balance of a magnetic torque generated by an external magnetic field (see Supporting Information and Figure S2) and a corresponding reaction torque from the constraint of the PDMS substrate (inset of Figure 2f). The reaction torque was obtained from finite element simulations (Abaqus), which show a linear relation between the reaction torque and the micropillar tilt angle θ (Figure 2f and Figure S3). Figure 2g shows that θ increases with both the magnetic field strength and field angle α. To measure the tilt angle of the fabricated μFUR, we applied the magnetic field using two parallel neodymium disc magnets (see Experimental Section and Figure S4). The magnetic field strength and field angle were determined by the orientation, diameter, thickness and spacing of the magnets. The experimental data shown in Figure 2g were taken when the magnetic field was kept at constant strength and field angles. The equilibrium tilt angle θ was obtained by side view microscope images of the pillar arrays (Figure 1d and 1e). The tilt angle response of the micropillars to a field angle change was instantaneous and no apparent hysteresis was observed over multiple measurement cycles due to the small hysteresis in the magnetization shown in Figure S1. Our experimental results are in excellent agreement with the model (Figure 2g), which demonstrates our ability to accurately control the micropillar tilt angle with an external field.

We show the versatility of our μFUR to dynamically manipulate liquid spreading, control fluid drag and tune optical transmittance. First, we demonstrate that we can achieve real-time

liquid directional spreading by dynamically changing the pillar tilt orientation and angle, where past studies have only shown uni-directional wetting in a fixed direction on static asymmetric structures.[6,7] We introduced a wetting liquid (30% IPA and 70% water), which satisfies the imbibition condition[28] to the surface through a syringe at a constant flow rate of 0.25 μL s^{-1} (**Figure 3**a and Supporting Information Video 3). The liquid film propagates only if the contact line is able to reach the next row of the pillars (inset of Figure 3a). Therefore, under the magnetic field, the asymmetric structures can initiate a preferential propagation direction (Figure S5), which is determined by the micropillar tilt angle, spacing and the intrinsic contact angle of the liquid on the surface.[6] The surface was initially subjected to a magnetic field tilted to the right (α = 60 °, $\mu_0 H$ = 0.5 T) and the fluid only flowed in the pillar tilt direction while being highly pinned in all other directions. At t = 2.5 s and t = 6.2 s, the direction of the magnetic field was switched. As a result the fluid instantaneously changed its propagating and pinning directions (Supporting Information Video 3). This dynamic manipulation can be achieved when the pillar tilt angle θ is above 12 ° for the test fluid (30% IPA and 70% water) which is determined by the pillar geometry and surface wettability, and agrees with a model developed by Chu *et al.* for static asymmetric structures.[6] Furthermore, this repeatable and instantaneous manipulation capability is not restricted to the $\pm x$ direction, but can be applied to all directions on the 2D surface, and even on a vertically inclined surface (Supporting Information Video 4).

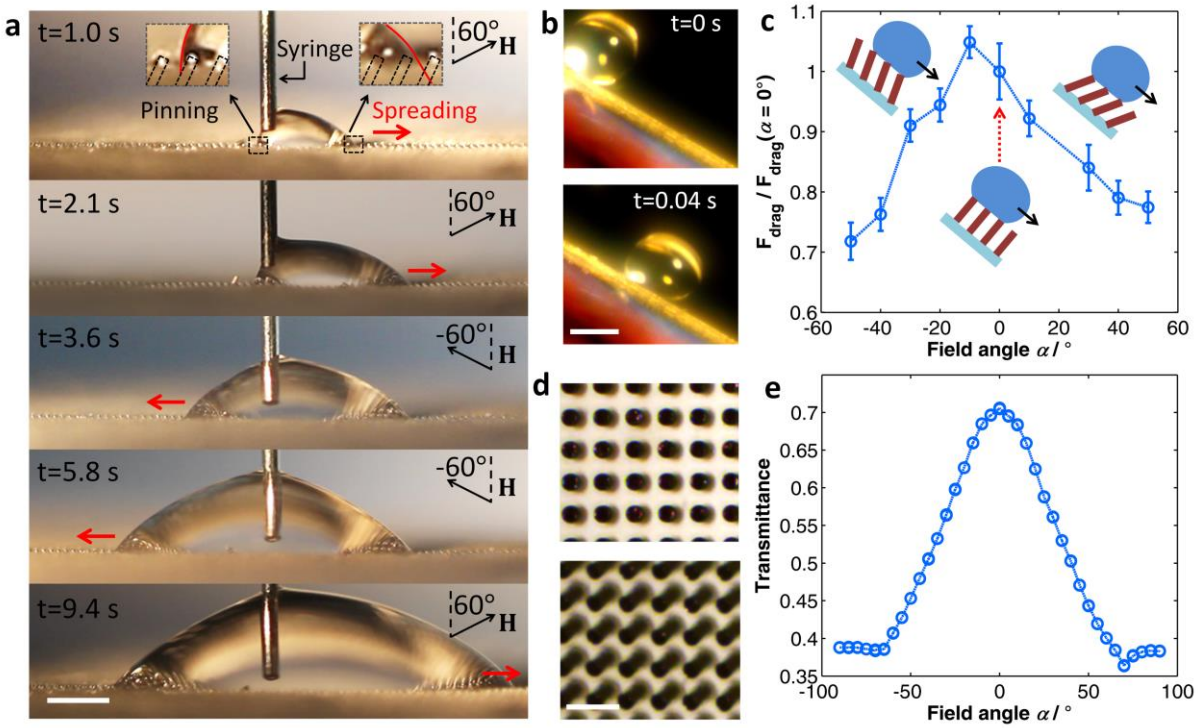

Figure 3. a) Fluid (30% IPA and 70% water) spreading direction is dynamically controlled while the fluid only propagates in the pillar tilt direction (red arrow) and is pinned in all other directions. The black dotted lines in the insets indicate the location of the micropillars and the red solid lines depict the liquid-air interface. Field strength is 0.5 T. Scale bar is 0.5 mm. b) Time-lapse images of a water droplet sliding on the μFUR with a tunable drag force. Scale bar is 2 mm. c) Normalized drag force as a function of the field angle. Field strength is 0.35 T. The negative sign represents that the tilt direction is against the sliding direction. Error bars account for the standard deviation of multiple measurements and an estimated system error. The maximum value of drag force at $\alpha = -10\,°$ shows no statistically significant difference when compared with the value at $\alpha = 0\,°$ (within the error bars). d) Top view images of the tunable surface with field angles of 5 ° and 70 °. Scale bar is 100 μm. e) Transmittance of a 635 nm laser as a function of the magnetic field angle. Magnetic field strength is 0.35 T. Error bars are approximately ±0.03 which account for standard deviation of multiple measurements and an estimated system error.

We also show that μFUR can tune the drag force with high surface tension fluids, *e.g.*, water. Past works have focused on reducing fluid drag with static hydrophobic microstructures.[29,30] In contrast, increasing the tilt angle of the μFUR decreases the effective fluid-surface contact area (solid fraction), and changes the fluid-solid interface morphology. We examined the sliding behavior of a water droplet (7 μL) on a tilted surface under various field angles (Figure 3b) at 0.35 T, the velocity and acceleration of which were extracted from the time-lapse images captured by a high-speed camera to obtain the drag force.

From the displacement data, *e.g.*, in Figure S6, the droplet experiences a short acceleration period after detaching from the needle, and then transitions to a steady deceleration mode due to the drag force. The acceleration originates from the deformation of the droplet shape which lowers its potential energy and is converted to kinetic energy. A second order polynomial relation between the displacement x and time t was observed for the deceleration mode, indicating a constant drag force for each situation, *i.e.*, $a = \mathrm{d}^2x/\mathrm{d}t^2$. The drag force, F_{drag}, is then determined based on a force balance,

$$ma = mg\sin(\beta) - F_{drag} \quad (1)$$

where β is the slope angle (40 °) and m is the mass of the droplet. We normalized the drag force with respect to the zero field angle case (α = 0 °) to facilitate a comparison. A maximum reduction in drag of 28% was observed at a field angle of −50° (Figure 3c and Supporting Information Video 5). The drag force decreases with an increase in tilt angle both against the flow and with the flow due to the effect of reduced solid fraction. The solid fraction at zero field angle can be changed by altering the geometry of the μFUR during fabrication. This, however, will only change the absolute drag force exerted on the droplet, where the relative trends with the dynamic tunability will remain the same.

The difference in the optical properties between the opaque pillar surface and the transparent PDMS film provides additional opportunities for dynamic optical tuning. This is typically difficult to achieve using hydrogel structures or PDMS structures mixed with magnetic particles because the refractive indices of the hydrogel and the surrounding liquid are similar, and usually both the substrate and the micropillars of the PDMS/magnetic particle mixtures have the same optical properties.[20,21] We demonstrated that by utilizing the asymmetry of the microstructures (Figure 3d and Supporting Information Video 2), the surface can function similar to 'window blinds', where the transmittance can be tuned on demand. We measured the transmitted power of a collimated laser beam (λ = 635 nm, spot size was 1.5 – 2 mm) through the sample using a photodiode detector (Figure S8 and Experimental Section). The transmittance of μFUR was calculated using the detected power of the laser beam through the sample and the glass normalized by that through the glass only. Transmittance of the μFUR ranging from 0.38 to 0.71 under different magnetic field angles at 0.35 T was observed (Figure 3e). The response is instantaneous and the results were repeatable. This work suggests that the surface has great potential in applications where manipulating both liquid and light is required.

We have demonstrated a tunable and controlled platform using simple fabrication approach, which has a large tuning range (0 - 57 ° tilt angles) with precise and continuous control. The versatile μFUR is capable of dynamic manipulation of fluid spreading directionality, fluid drag, and can tune optical transmittance over a large range by adjusting the applied magnetic field. This work provides exciting opportunities for real-time fluid and light manipulation. Biomimetic functionalities such as locomotion and liquid or cell transport can potentially be achieved by applying localized and variable magnetic fields. It will also be of significant interest as the size of the micropillars is scaled down to the order of the wavelength of visible

light, when the structures can coherently manipulate light propagation and act as tunable photonic crystals. By tuning the geometry, wettability, optical properties and surface chemistry of the micropillars and the substrate, the surface can expand its manipulation capabilities, and serve as an important platform for applications such as smart window, versatile artificial skin, cell manipulation, dynamic optical devices and fluid control. In applications with high curvature and complex shaped substrates, a modified distribution of the magnetic field may be applied to achieve the desired tilt angle.

Experimental Section

Tilt Angle Measurement: The experimental setup to measure the tilt angle is illustrated in Figure S4. An optical microscope was used to capture the side view images of the pillar arrays. The μFUR is attached to a glass slide, which is inserted into a cylindrical Teflon sample holder. To provide an external magnetic field, the sample was placed between two neodymium disc magnets (Grade N52, K&J Magnetics, Inc.) which were placed parallel to each other on the two arms of a steel clevis. The clevis was inserted into a ball bearing so that the attached magnets could be rotated around the sample surface while maintaining a constant field strength during rotation. The magnetic field orientation was controlled by rotating the clevis, and the magnetic field strength was calculated by K&J Magnetics Gap Calculator (K&J Magnetics) based on the diameter, thickness and gap. Tilt angles in magnetic field of 0.35 T and 0.5 T were measured as a function of field angles.

Drag Force Measurement: To measure the drag force, we examined the sliding behavior of a water drop (7 μL) on a tilted μFUR surface (40°) under various field angles and a field strength of 0.35 T. The initial condition was kept the same for all of the experiments. DI water supplied by a syringe at a fixed flow rate of approximately 2.5 μL s^{-1} was used as the test fluid.

The distance between the syringe needle and the tunable surface was adjusted such that the droplet just touched the surface when it detached from the needle. High-speed camera imaging (Phantom v7.1, Vision Research) at 500 frames s^{-1} was used to capture the droplet displacement x as a function of time t (Figure S6 and S7).

Transmittance Measurement: The experimental setup to measure transmittance is illustrated in Figure S8. Two mirrors at an angle of 90 ° were attached to the sample holder with one 45 ° above the horizontal and the other 45 ° below the horizontal. The tunable surface sample was placed on a horizontal glass slide between the two mirrors. A laser with a 635 nm wavelength (LTG6351AH, Lasermate Group, Inc.) was used as the light source for the measurement. The laser had an elliptical beam profile (3.3 mm × 3.6 mm), and was well-collimated with a beam divergence of less than 0.5 mrad. An iris (ID-1.0, Newport) was used to define a circular spot shape of the laser beam. The beam diameter of the laser after the iris was 1.5 - 2 mm. The laser was adjusted such that the beam was horizontal and transmitted through the tunable surface as indicated by Figure S8. The distance between the laser source and the sample was approximately 13 cm. A third mirror was used to reflect the transmitted laser beam to a photodiode detector (818UV, Newport) connected to a power meter (1918C, Newport). The transmittance of μFUR was calculated using the detected power of the laser beam through the sample and the glass substrate normalized by that through the glass only. The measured transmittance through the fabricated PDMS substrate was 0.91 ±0.03.

Acknowledgements

We thank D. Kim and C. Ross for use of VSM equipment; K. Wang and T. Wierzbicki for help with Abaqus simulation; J. Tong for use of laser equipment; K.-H. Chu, Y. Nam, Y. Yang and P. Kim for discussion. We gratefully acknowledge funding support from the Air Force Office of Scientific Research (AFOSR, Grant FA9550-11-1-0059). We would also like to acknowledge the MIT Microsystems Technology Lab for fabrication staff support, help, and use of equipment.

[1] E. Martines, K. Seunarine, H. Morgan, N. Gadegaard, C. D. W. Wilkinson, M. O. Riehle, *Nano Lett.* **2005**, 5, 2097.

[2] L. Qu, L. Dai, M. Stone, Z. Xia, Z. L. Wang, *Science* **2008**, 322, 238.

[3] K.-C. Park, H. J. Choi, C.-H. Chang, R. E. Cohen, G. H. McKinley, G. Barbastathis, *ACS Nano* **2012**, 6, 3789.

[4] F. Priolo, T. Gregorkiewicz, M. Galli, T. F. Krauss, *Nat. Nanotechnol.* **2014**, 9, 19.

[5] A. Lenert, D. M. Bierman, Y. Nam, W. R. Chan, I. Celanović, M. Soljačić, E. N. Wang, *Nat. Nanotechnol.* **2014**, doi:10.1038/nnano.2013.286.

[6] K.-H. Chu, R. Xiao E. N. Wang, *Nat. Mater.* **2010**, 9, 413.

[7] N. A. Malvadkar, M. J. Hancock, K. Sekeroglu, W. J. Dressick, M. C. Demirel, *Nat. Mater.* **2010**, 9, 1023.

[8] H. E. Jeong, M. K. Kwak, K. Y. Suh, *Langmuir* **2010**, 26, 2223.

[9] D. Santos, S. Kim, M. Spenko, A. Parness, M. Cutkosky, in *2007 IEEE Int. Conf. Robot. Autom.* **2007**, 1262, doi:10.1109/ROBOT.2007.363158.

[10] S. Reddy, E. Arzt, A. del Campo, *Adv. Mater.* **2007**, 19, 3833.

[11] R. Yoshida, K. Uchida, Y. Kaneko, K. Sakai, A. Kikuchi, Y. Sakurai, T. Okano, *Nature* **1995**, 374, 240.

[12] X. He, M. Aizenberg, O. Kuksenok, L. D. Zarzar, A. Shastri, A. C. Balazs, J. Aizenberg, *Nature* **2012**, 487, 214.

[13] J. Cui, D.-M. Drotlef, I. Larraza, J. P. Fernández-Blázquez, L. F. Boesel, C. Ohm, M. Mezger, R. Zentel, A. del Campo, *Adv. Mater.* **2012**, 24, 4601.

[14] L. D. Zarzar, P. Kim, J. Aizenberg, *Adv. Mater.* **2011**, 23, 1442.

[15] T. Tanaka, D. Fillmore, S.-T. Sun, I. Nishio, G. Swislow, A. Shah, *Phys. Rev. Lett.* **1980**, 45, 1636.

[16] D. J. Beebe, J. S. Moore, J. M. Bauer, Q. Yu, R. H. Liu, C. Devadoss B.-H. Jo, *Nature* **2000**, 404, 588.

[17] P. J. Glazer, J. Leuven, H. An, S. G. Lemay, E. Mendes, *Adv. Funct. Mater.* **2013**, 23, 2964.

[18] J. Kim, S. E. Chung, S.-E. Choi, H. Lee, J Kim, S. K. Kim, *Nat. Mater.* **2011**, 10, 747.

[19] N. J. Sniadecki, A. Anguelouch, M. T. Yang, C. M. Lamb, Z. Liu, S. B. Kirschner, Y. Liu, D. H. Reich, C. S. Chen, *Proc. Natl. Acad. Sci.* **2007**, 104, 14553.

[20] A. R. Shields, B. L. Fiser, B. A. Evans, M. R. Falvo, S. Washburn, R. Superfine, *Proc. Natl. Acad. Sci.* **2010**, 107, 15670.

[21] F. Fahrni, M. W. J. Prins, L. J. van IJzendoorn, *Lab. Chip* **2009**, 9, 3413.

[22] J. V. I. Timonen, C. Johans, K. Kontturi, A. Walther, O. Ikkala, R. H. A. Ras, *ACS Appl. Mater. Interfaces.* **2010**, 2, 2226.

[23] D.-M. Drotlef, P. Blümler, A. del Campo, *Adv. Mater.* **2014**, 26, 775.

[24] R. M. Macnab, *J. Bacteriol.* **1999**, 181, 7149.

[25] Y. Enuka, I. Hanukoglu, O. Edelheit, H. Vaknine, A. Hanukoglu, *Histochem. Cell Biol.* **2012**, 137**,** 339.

[26] N. C. Turner, P. J. Kramer, *Adaptation of Plants to Water and High Temperature Stress*, J. Wiley, **1980**.

[27] P. F. Scholander, V. Walters, R. Hock, L. Irving, *Biol. Bull.* **1950**, 99, 225.

[28] J. Bico, C. Tordeux, D. Quéré, *EPL Europhys. Lett.* **2001**, 55, 214.

[29] F. Shi, Z. Wang, X. Zhang, *Adv. Mater.* **2005**, 17, 1005.

[30] W. Barthlott, T. Schimmel, S. Wiersch, K. Koch, M. Brede, M. Barczewski, S. Walheim, A. Weis, A. Kaltenmaier, A. Leder, H. F. Bohn, *Adv. Mater.* **2010**, 22, 2325.

Supporting Information

Real-Time Manipulation with Magnetically Tunable Structures

*Yangying Zhu, Dion S. Antao, Rong Xiao, Evelyn N. Wang**

Sample Fabrication

A 100 nm gold layer was deposited on top of a 20 nm titanium adhesion layer as the main seed layer on a 6 inch silicon substrate by e-beam thermal evaporation. A 100 μm thick negative photoresist (KMPR 1050, MicroChem) layer was spin-coated on the seed layer at 1300 rpm for 30 s, soft baked on a hotplate at 100 ℃ for 27 min, exposed to UV illumination at 750 mJ cm^{-2}, post baked at 100 ℃ for 6 min and developed for 15 min. The result was a thick photoresist layer with uniform hole arrays. The wafer was then diced into 2×2 cm^2 samples. To remove air trapped in the hole arrays of the photoresist, the sample was treated with oxygen plasma (29 W at 500 mTorr for 30 min) and sonicated in the plating solution for 45 s. A dense array of nickel pillars was subsequently obtained by electroplating (Nickel Sulfamate RTU, Technic Inc.) at 50 ℃ for 6 hours with a current density of 13 mA cm^{-2}. The patterned photoresist surface was lifted by immersing in acetone (room temperature, 8 hours) and in MicroChem Remover PG (70 ℃, 2 hours). Photoresist residue was oxidized by sodium permanganate and dissolved in methane sulfonic acid. The sample was rinsed with DI water. A ~10 nm silica layer was deposited on the pillar tips by plasma-enhanced chemical vapor deposition (PECVD). A 100 μm PDMS layer was spin-coated on a glass substrate, cured, and oxygen plasma treated (29 W at 500 mTorr for 10 min). The nickel pillars coated with silica on the tips were subjected to the same plasma treatment conditions and bonded onto the PDMS surface. The sample was immersed in a nickel compatible gold etchant (Sigma-Aldrich) and degased. The solution was then heated to 70 ℃ on a hotplate for 2 hours to etch away the gold seed layer such that the pillars (detached from the silicon substrate) remained

only on the PDMS substrate.

Magnetic Properties of Electroplated Nickel

After the photoresist removal, we characterized the magnetic properties of the pillar arrays using vibrating sample magnetometer (VSM), and confirmed that they match the properties of bulk nickel with a coercivity of 60 Oe (4.8×10^3 A m^{-1}). The measured magnetization M is normalized with respect to the saturation value (M_{sat} = 0.6 T for nickel). Magnetization saturates at an applied magnetic field strength of 0.3 T (Figure S1). The measured magnetization is used in the model to calculate the magnetic torque and to calculate the tilt angle θ.

Model

The model consists of 80 μm nickel pillars attached to a layer of 100 μm soft PDMS layer with the fabricated pillar geometry and magnetic properties, where the bottom surface of the PDMS layer was fixed. The magnetic torque is given by Equation S1,

$$T_{mag} = V\mathbf{M}\times\mathbf{B} \quad \text{(S1)}$$

where V is the volume of the magnetic pillar, **M** is the magnetization of the nickel micropillars which is assumed to be in the axial direction, and **B** is the magnetic flux density.

Considering the pillar geometry, applied field strength and field angle, the magnetic torque can be calculated as,

$$T_{mag} = \frac{\pi}{4} d^2 h M \mu_0 H \sin(\alpha - \theta) \quad \text{(S2)}$$

where d and h are the diameter and height of the pillars, M is the magnitude of magnetization, μ_0 is the vacuum permeability, H is the magnitude of the applied field, α is the field angle

defined as the angle between the applied field and the surface vertical direction, and θ is the pillar tilt angle. Figure S2 shows the magnetic torque as a function of the tilt angle θ according to Equation S2. T_{mag} increases with the magnetic field strength and field angle.

The relationship between the reaction torque and the tilt angle was obtained using finite element simulations (Abaqus). The model consists of a 100 μm thick PDMS substrate with the bottom surface fixed. Five pillars were built in the model and we assume that the periodic boundary conditions are valid for the pillar in the center. The nickel pillars (heights h = 80 μm, diameters d = 26 μm, spacings l = 60 μm) were adhered to the PDMS layer with 60 μm above the PDMS surface and 20 μm embedded in the PDMS layer. Contact surfaces between the PDMS and the pillars were tied together. A torque was applied on each micropillar (clockwise). All other surfaces are free surfaces. An equilibrium tilt angle of the pillar in the center was captured by the model under each applied torque ranging from 0 N·m to 3.5×10^{-9} N·m (Figure 2f). Figure S3 shows an example of the model when the applied torque is 3.5×10^{-9} N·m. The reaction torque $T_{reaction}$ from the PDMS has the same magnitude as the applied torque at equilibrium.

The tilt angle θ of the micropillars under an applied magnetic field was calculated by solving Equation S3, which is a torque balance equation between the magnetic torque and the reaction torque.

$$T_{mag}(\theta, H, \alpha) = T_{reaction}(\theta) \quad \text{(S3)}$$

The final result can be expressed as $\theta = f(H, \alpha)$, as shown in Figure 2g.

Drag Force Calculation

To compare the effect of the magnetic field angle α on the drag force, we normalized F_{drag} as

shown in Equation S4,

$$\frac{F_{drag}(\alpha)}{F_{drag}(\alpha = 0°)} = \frac{g\sin(\beta) - a(\alpha)}{g\sin(\beta) - a(\alpha = 0°)} \quad \text{(S4)}$$

where β is the slope angle. Figure S7 and Supporting Information Video 5 show a higher deceleration at $\alpha = -20°$ than $\alpha = -50°$, indicating a higher drag force at $\alpha = -20°$. When $\alpha = -50°$, the displacement is approximately linear with time, indicating a reduced drag force close to $mg\,sin(\beta)$.

Supporting Information Figures

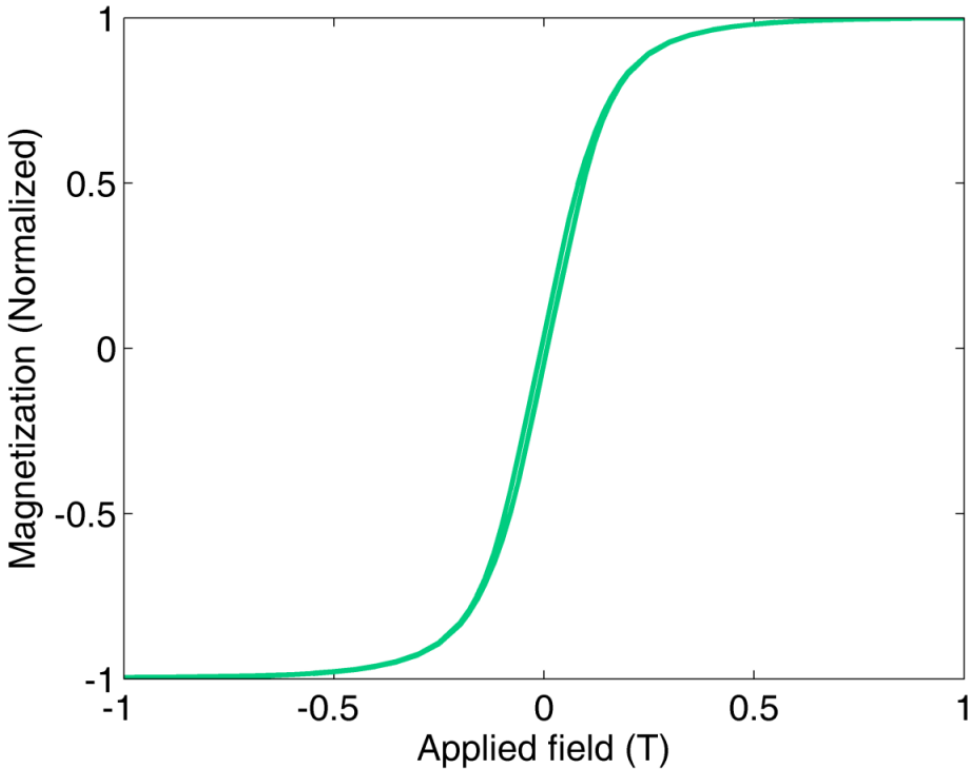

Figure S1 Normalized magnetization of the electroplated nickel pillar arrays measured by vibrating sample magnetometer. The magnetization is normalized with respect to the saturation magnetization (M_{sat} = 0.6 T for nickel). The measured magnetization is used in the model to calculate the magnetic torque given by Equation S2 and to calculate the tilt angle θ.

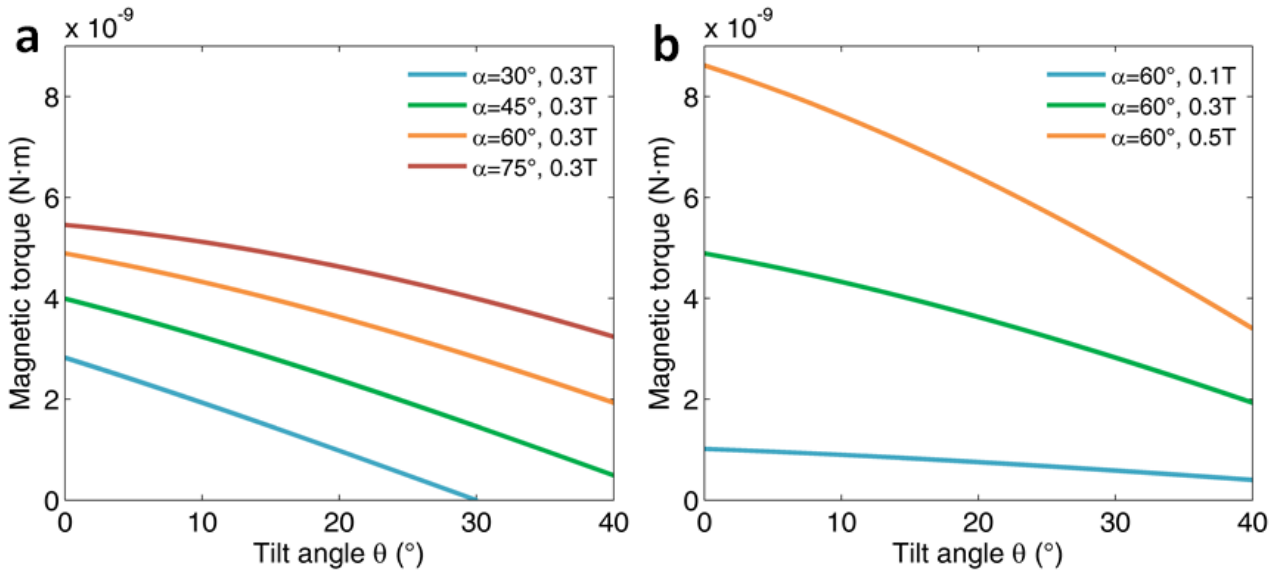

Figure S2 Magnetic torque as a function of tilt angle under different a) magnetic field angles and b) field strength based on Equation S2. Magnetic torque increases with both magnetic field angle and field strength.

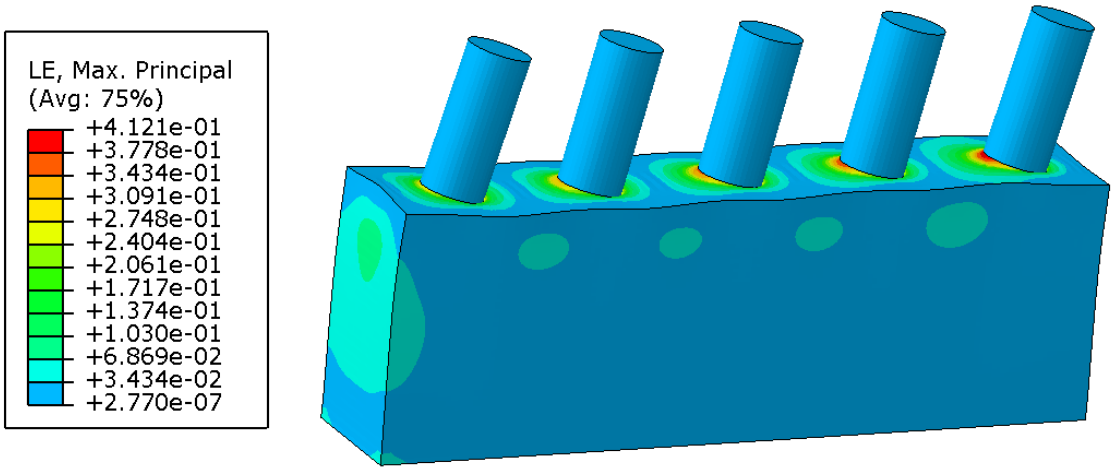

Figure S3 Finite element simulation (Abaqus) of the micropillar tilt angles. The PDMS substrate is 100 μm thick with the bottom surface fixed. Five nickel pillars (heights h = 80 μm, diameters d = 26 μm, and spacings l = 60 μm) were adhered to the PDMS layer with 60 μm above the PDMS surface and 20 μm embedded in the PDMS. A torque of 3.5×10^{-9} N m was applied on each micropillar (clockwise). All other surfaces are free. Legend represents the logarithmic principle strain.

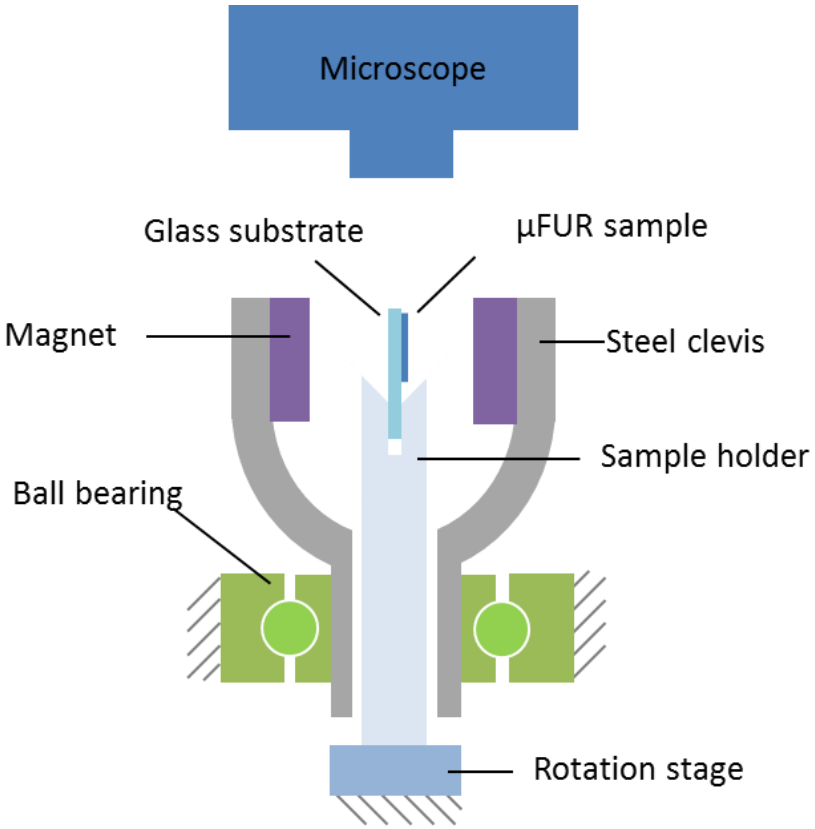

Figure S4 Schematic of the tilt angle measurement system. The tunable surface was attached to a glass slide, which was inserted into a cylindrical Teflon sample holder. To generate an external magnetic field, the sample was placed between two neodymium disc magnets which were placed parallel to each other on the two arms of a steel clevis. The clevis was inserted into a ball bearing so that the attached magnets could be rotated around the sample surface while maintaining a constant field strength during rotation.

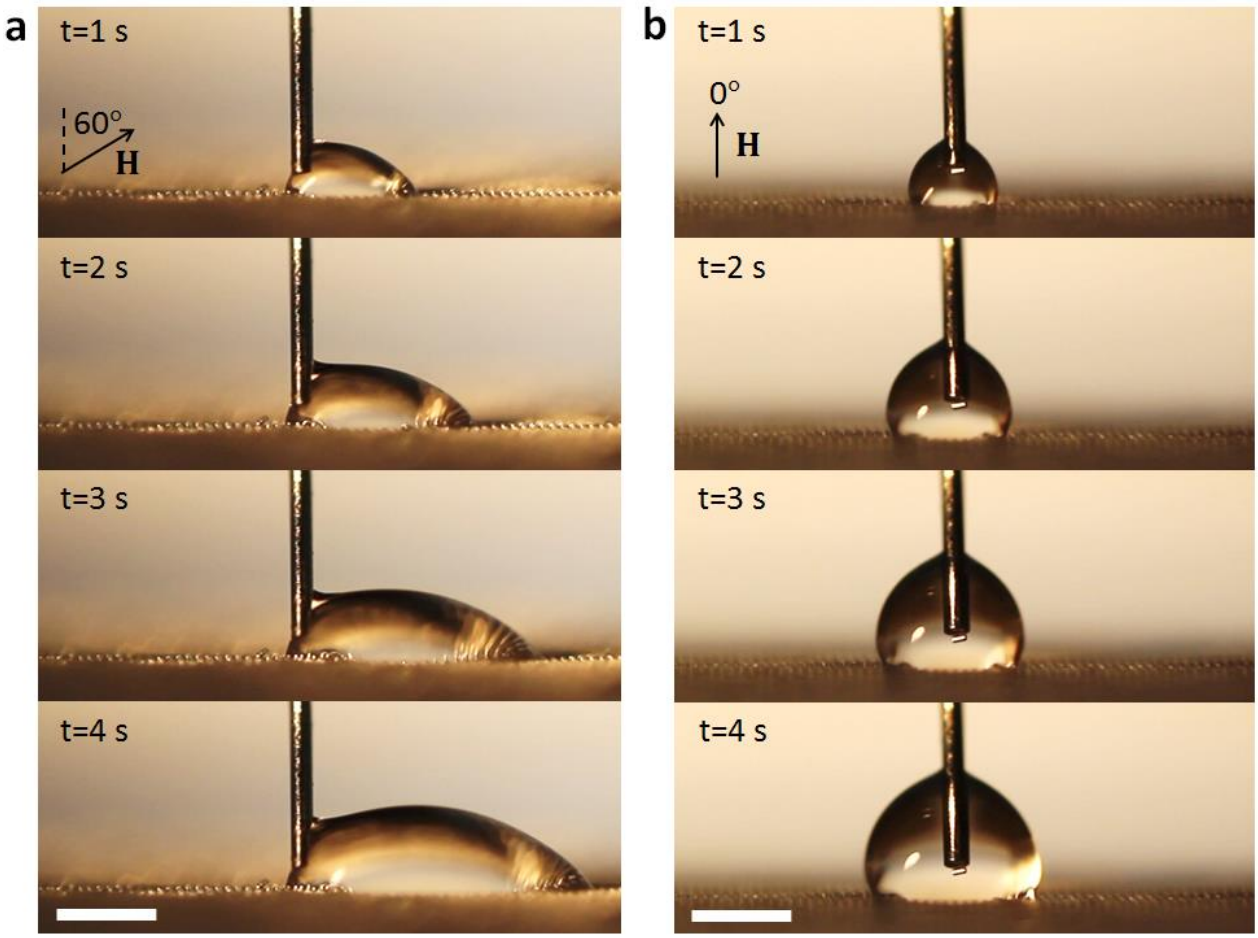

Figure S5 Time-lapse images of a fluid (30% IPA and 70% water) spreading on μFUR under two different magnetic field directions. The magnetic field strength is 0.5 T. a) Magnetic field angle is 60 °. The fluid spreads to the right and is pinned in all other directions. b) Magnetic field angle is 0 °. The fluid spreads in all directions. Scale bar is 0.5 mm.

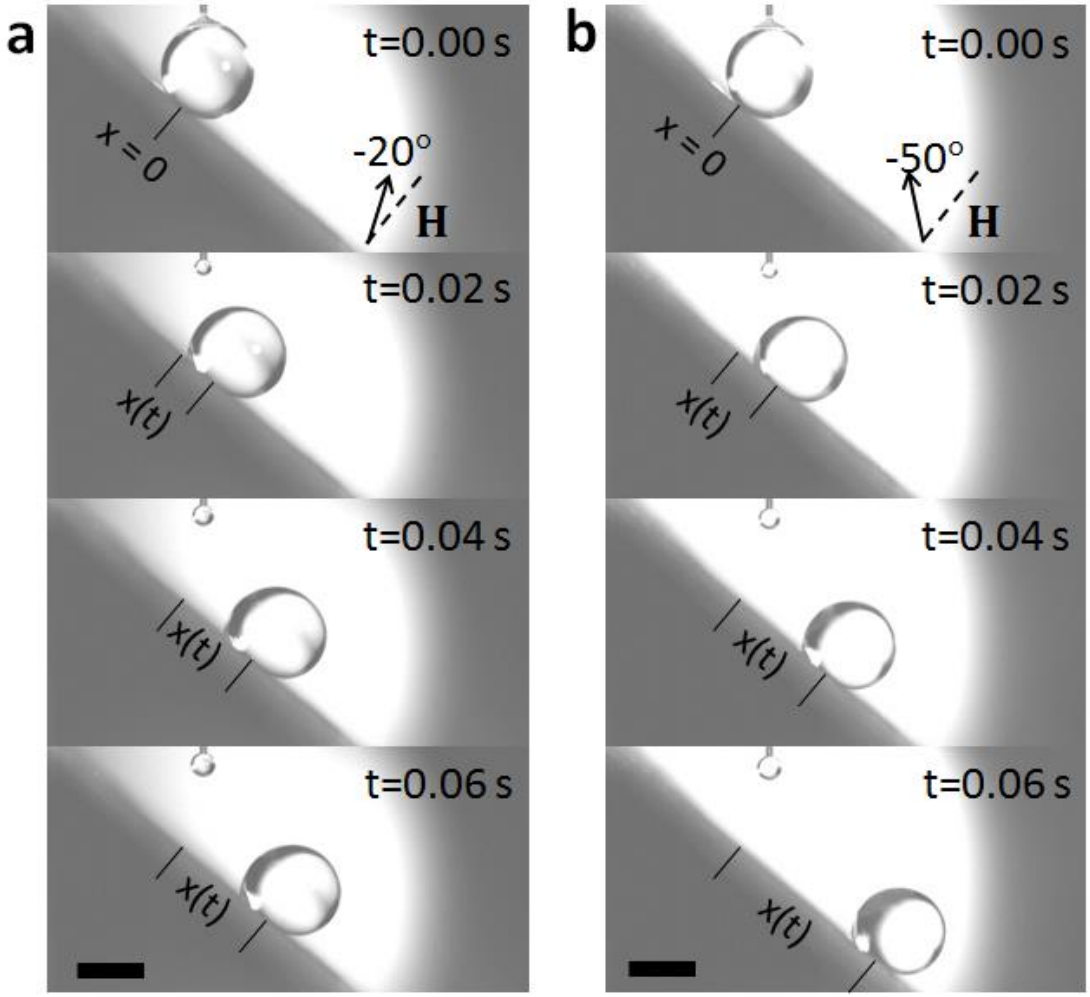

Figure S6 Time-lapse high-speed camera images of a water droplet sliding on μFUR (tilted at 40 °) under a magnetic field of 0.35 T at two different field angles. a) Magnetic field angle is −20 °. b) Magnetic field angle is -50 °. Droplet position *x* can be extracted as a function of time *t*. The displacements indicate a reduced drag force at α = -50 ° compared to α = -20 °. Scale bars are 2 mm.

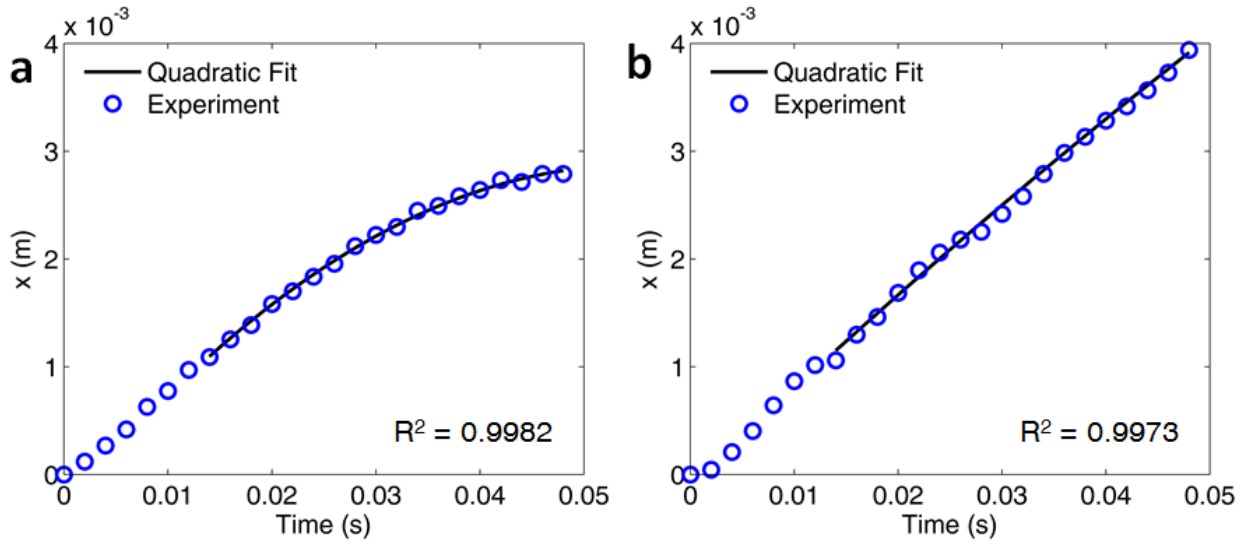

Figure S7 Water droplet sliding displacement x as a function of time on the tunable surface with a 0.35 T magnetic field and field angles of a) $\alpha = -20\,°$ and b) $\alpha = -50\,°$. The droplet experiences a short acceleration period after detaching from the needle, and then transitions to a steady deceleration mode due to the drag force. A second order polynomial relation between the displacement x and time t was observed for the deceleration mode ($t > 0.014$ s), indicating a constant drag force for each situation. The displacements indicate a reduced drag force at $\alpha = -50\,°$ compared to $\alpha = -20\,°$.

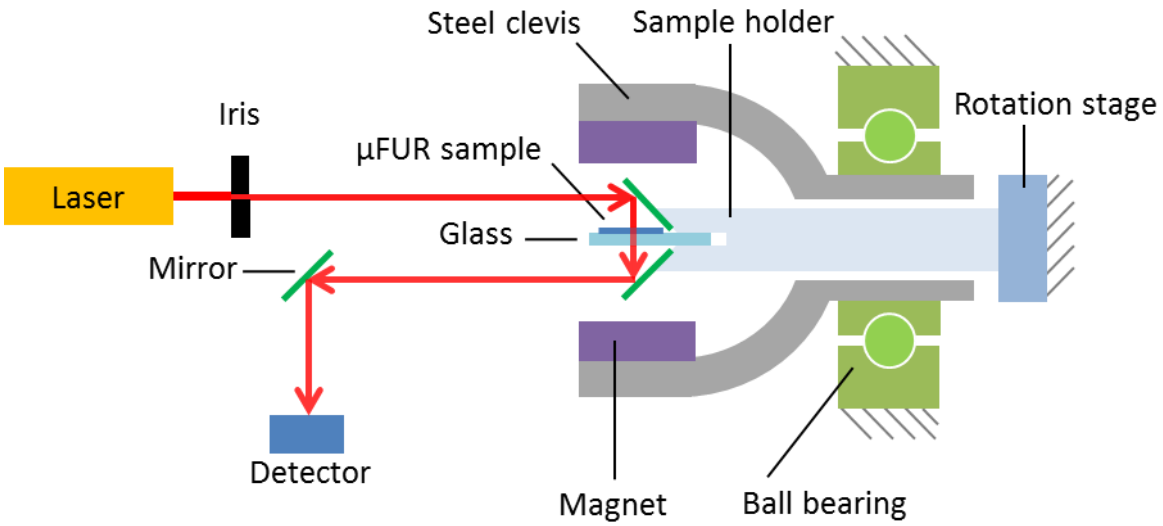

Figure S8 Schematic of transmittance measurement system. Two mirrors at an angle of 90 ° were attached to the sample holder with one 45 °above the horizontal and the other 45 °below the horizontal. The tunable surface sample was placed on a horizontal glass slide between the two mirrors. A laser with 635 nm wavelength (LTG6351AH, Lasermate Group, Inc.) was used as the light source for the measurement. The laser was adjusted such that the beam was horizontal and transmitted through the tunable surface. A photodiode detector (818UV, Newport) connected to a power meter (1918C, Newport) was used to measure the transmitted power.